This is the author's accepted, refereed and final manuscript of the article:

A Lagrangian study of liquid flow in a reverse-flow hydrocyclone using positron emission particle tracking

A Lagrangian study of liquid flow in a reverse-flow hydrocyclone using positron emission particle tracking

Yu-Fen Chang · **Alex C. Hoffmann**

Abstract In this study the liquid flow in a reverse-flow hydrocyclone is studied experimentally using the Lagrangian approach. Resin beads with densities that are close to the density of the liquid in which they move, i.e. neutral-density particles, are used to model a fluid element in the highly turbulent flow in a hydrocyclone separator and tracked using PEPT with a temporal resolution of up to 0.5 ms. A method of producing neutral-density particles for PEPT was developed. The data processing algorithm was improved for the extra challenging tracking conditions that were encountered. The components of velocity, which reveal the detailed velocity field of the fluid, were calculated from the positions of the tracers. Various noise-removal methods, again to cope with the challenging tracking conditions, were applied and discussed.

1 Introduction

1.1 Hydrocyclones

Hydrocyclones, as shown in Fig. 1, are solid/liquid or liquid/liquid separators utilizing the "centrifugal force" to

Y.-F. Chang
Department of Physics and Technology, University of Bergen, Allegaten 55, 5007 Bergen, Norway
Tel.: +47 97478411
E-mail: yu-fen.chang@ift.uib.no

A.C. Hoffmann
Department of Physics and Technology, University of Bergen, Allegaten 55, 5007 Bergen, Norway
Tel.: +47 55582876
Fax: +47 55589440
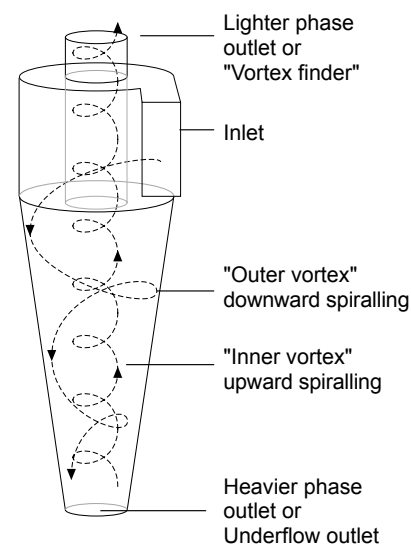E-mail: alex.hoffmann@ift.uib.no

Fig. 1 A schematic tangential-inlet cyclone with the cylinder-on-cone design, showing inlet, lighter and heavier phase outlet, as well as the vortex swirling downward in the outer region and upward in the centre.

separate mixtures composed of immiscible substances of different densities. The mixture is caused to swirl in the separation space, often by being injected tangentially. The denser component is flung onto the wall because of the rotation and transported to the underflow outlet. The lighter component moves to the centre where axial direction of the flow is upward, forming an "inner vortex", and escapes through the vortex finder (also called overflow outlet). Turbulence and flow instability in such complex flow field may well happen and affect the separation performance. For instance, it has been reported in Ref. [10] that a particle larger than the cut-size on its way to the underflow was rerouted in the wrong direction many times, which is likely due to a localised instability in the flow field.

1.2 Eulerian and Lagrangian flow visualization methods

Flow visualization improves the understanding of flows both in areas of fundamental science, such as fluid mechanics and rheology, and in areas of engineering, such as the design of process equipment. Techniques looking at fluid motion at specific locations, e.g. particle image velocimetry (PIV) and laser Doppler anemometry (LDA), provide Eulerian representations of the flow. For instance, velocity profiles and turbulence production in a hydrocyclone have been measured using LDA [9, 14, 16, 20]. Velocity vector fields in a hydrocyclone have also been obtained using PIV [25]. The time-averaged velocity field, however, cannot reveal the unsteady flow field associated with the "precession of the vortex core" or the "end of the vortex," which has been observed at certain positions in gas cyclones (e.g. [17, 29]) and hydrocyclones (e.g. [10]).

Techniques that follow an individual particle or fluid element as it moves through space and time give the pathlines, which are Lagrangian representation of the flow. The pathlines can greatly help identifying regions with fluctuating and abnormal flow, as well as understanding complex flow patterns and mixing of flows [3, 12]. Techniques being able to precisely record the tracks in the complex flow are therefore found very important. This study aims to observe the fast and strongly swirling flow in a hydrocyclone by following the history of a fluid element, i.e. using the Lagrangian tracking method.

Positron emission particle tracking (PEPT), a technique that follows the motion of one or more particles, has been used to investigate the movement of solid particles in a variety of multiphase processes (see, e.g., Ref. [23, 28]). The tracer particles are labelled with positron emitting isotopes. The positron, after having been emitted from a nucleus of the tracer material, annihilates with an electron within a few millimeter, and the annihilation produces two gamma photons which propagate in back-to-back directions, i.e. at approximately 180 degrees to each other. After a gamma-photon pair has been detected within a very narrow time-window, the tracer is known to locate on the line connecting the detector pair, forming a so-called line of response (LOR). Ideally the tracer location can be nearly identified at the cross-point of two subsequent LORs. However, a number of factors reduce the precision of the LOR location [2], and therefore reducing the errors by improving hardware and data processing methods is being investigated continuously. Recent improvements to the precision of PEPT have made it effective in tracking a fast-moving particle in highly turbulent flow with spatial resolution of 0.7 mm and temporal resolution of 0.5 ms [11]. In this study, high-resolution PEPT is employed for tracking fluid elements.
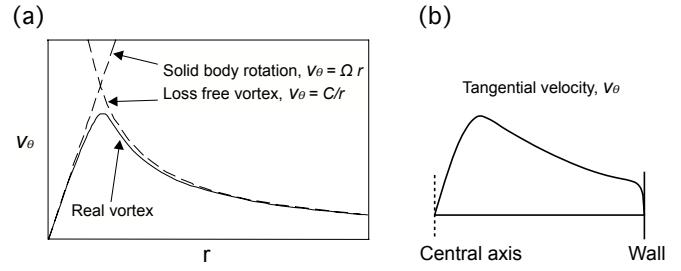

Fig. 2 (a) The dashed lines showing the two ideal vortex flows, and the solid line showing the tangential velocity distribution in a real vortex. (b) The radial distribution of the tangential velocity component in cyclones: a core of near solid-body rotation surrounded by a region of near loss-free rotation.

In general, in both Eulerian and Lagrangian approaches, tracer particles are frequently utilized to characterize fluid flows, assuming they closely follow the flow. However, due to the density difference between the particles and the fluid, the particles may behave differently, this is especially a problem in inertial separators. In fact, a solid particle will normally move relative to the fluid, whereas a fluid element moves exactly with the flow, reflecting the instantaneous fluid field. The difference become prominent in turbulent, high-speed, and swirling flows. Observing the movements of fluid elements in such flows, which are inherent to many processes and apparatuses, has been a need, yet a challenge. In this study we aim to develop a technique to visualize the paths of "fluid elements" with sufficient resolution for revealing details in highly turbulent and fast flows.

1.3 Velocity distribution

Much effort has been devoted to establish mathematical models for predicting and describing velocity distributions in cyclones, which are then to be used to derive the separation performance. The tangential velocity distribution in a real vortex comprises two types of nearly ideal swirling flows (see Fig. 2 (a)):

- nearly forced vortex flow or "solid-body rotation" in the centre,

$$v_\theta = \Omega r \qquad (1)$$

where Ω is angular velocity measured in radians per unit of time and v_θ is the tangential velocity, and
- nearly free vortex flow in the outer regions

$$v_\theta = \frac{C}{r} \qquad (2)$$

where C is a constant.

A vortex with solid-body rotation in the center surround by a loss-free rotation is called Rankine vortex.

Due to some loss caused by wall friction, the tangential velocity profile in a cyclone deviates slightly from a Rankine vortex, as shown in Fig. 2 (b). Alexander [1] gave a modified form describing the near loss-free part of the vortex:

$$v_\theta = \frac{C}{r^n} \qquad (3)$$

where the swirl velocity at the wall is often assumed as being equal to the inlet velocity in cyclones with tangential inlets. Once the swirl velocity at the wall is known, the tangential velocity at another radius can be calculated.

Tangential velocity profiles in hydrocyclones have been measured, for example, by intrusive probes [7] and optical methods [20, 22, 14, 21]. Knowles et al. obtained the tangential velocity profiles of anisole droplets with a density of 993 kg/m^3 in a hydrocyclone without an air-core using cine photography [22]. The value of n in Eq. (3) was determined as between 0.2 and 0.4. The region of "forced vortex flow" was not well defined in this study. Dabir and Petty used LDA to measure the tangential velocity profiles in a hydrocyclone operated with 20% underflow and without an air-core [14]. A forced vortex flow was measured close to the central axis and the n in Eq. (3) was determined to be 0.62. Hwang et al. obtained the tangential velocity profiles by using laser Doppler velocimetry (LDV) in a hydrocyclone without an air-core [21]. These studies all show that, beneath the vortex finder, the tangential velocity is almost solely related to the distance from the cyclone axis, i.e. it is similar at any height. Starting from the central axis of the cyclone, the tangential velocity, as observed in Ref. [14, 21], increases proportionally with the radius until reaching a maximum value at a radius somewhat smaller than the radius of the vortex finder. After this maximum value, the tangential velocity decreases as radius increases. It has been shown that, as the hydrocyclones are used in the paper industry, the presence of cellulose pulp fibers in the fluid lowered the maximum tangential velocity and smoothed the transition between the forced vortex and free vortex flow [5]. While most measurements in hydrocyclones, using e.g. optical, acoustic, and pressure techniques, were only conducted in lightly seeded or pure liquid due to experimental difficulties, PEPT can easily be applied to investigate the flow field under a varying solids loading.

2 Experimental

2.1 Liquid flow system incorporating a hydrocyclone separator

A hydrocyclone for solid/liquid separation, the dimensions of which are shown in Fig. 3 (b), was incorporated in a liquid flow system as shown in Fig. 3 (a). The hydrocyclone
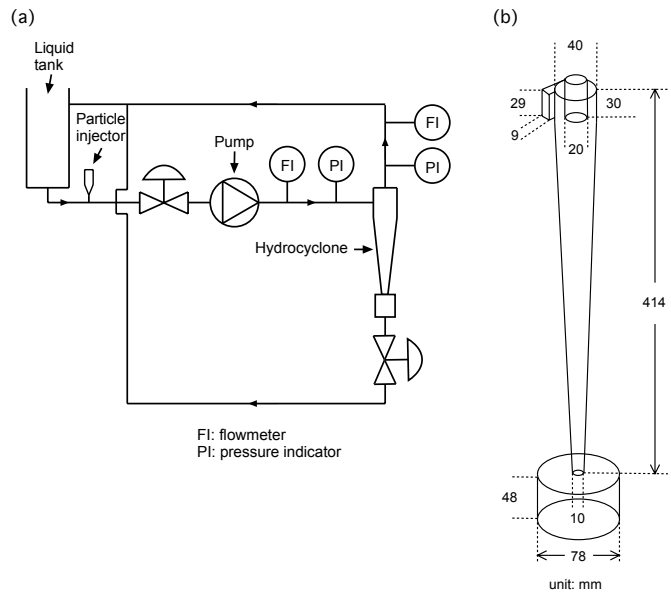

Fig. 3 (a) A diagram showing the liquid flow system incorporating a hydrocyclone separator. (b) Dimensions of the hydrocyclone used in this study.

used in this work is an analogue of a type of desanding hydrocyclones. The inlet velocity can be adjusted by the pump and a valve upstream of the inlet. The flow fraction through the two outlets can be adjusted by a valve on the underflow outlet. In normal use of a hydrocyclone, the products from the two outlets are to be collected separately. But since in these experiments, we are interested in the flow patterns rather than the separated products, the overflow and underflow were routed back to the tank. The hydrocyclone was therefore operated without an air-core due to the water-sealed underflow outlet. The flow rates at the inlet and the overflow were measured by the transit-time ultrasonic flowmeter, the Innova-Sonic Model 206 In-line (Sierra Instruments).

2.2 Neutral-density particle tracer

As mentioned in Sect. 1, in PEPT the tracer needs to be activated by labeling with positron emitting isotopes. In our experiments, the porous-structured strong-based anion ion exchange resin beads, Amberlyst A26 OH form (Acros Organics), with harmonic mean size of 560–700 μm, were labeled with ^{18}F. Firstly ^{18}F ions were generated in water by ^{18}O(p,n)^{18}F nuclear reaction in cyclotron. Secondly the resin beads were immersed into the radioactive water and the mixture was shaken for about 10 min. The ^{18}F bound to the bead material by ion exchange with the OH group. The resulting radioactivity on each bead can reach 450–1440 μCi, depending on the ^{18}F concentration in water and the size of the bead. Dissociation and dispersion of ^{18}F in water were checked by the uncertainty in positioning

a stationary tracer as function of time (see Sect. 2.3 and Ref. [10]).

In order that the particles follow the fluid flow, the particles have to be made neutrally buoyant in the fluid, i.e. the particles will neither float nor sink in the fluid. This can be achieved by adjusting the relative densities of the particle and fluid. The density of the resin beads in water is around 1080–1120 kg/m^3 measured by free settling in water. One way to adjust the relative density is to increase the density of the fluid. For instance, in Ref. [8, 32] the mixture compositions of the fluid were tuned to match the density of tracers in order to make the tracers neutrally buoyant. Glycerin and sugar are convenient density modifiers for water because of their known properties of water solutions and because they are rather safe to handle. However, both of them also alter the viscosity, which then alters the flow pattern that we intend to observe. Taking the safety, as well as changes in density and viscosity into consideration, salt, i.e. NaCl, was chosen as an additive to modify the density, as the viscosity of salt solutions is not much changed when its density approaches the density of the resin beads. At 20 degree Celsius and density of 1100 kg/m^3, the viscosity of water solutions of NaCl, glycerin, and sugar are about 1.3, 3.5 and 2.4 cp, respectively [24, 13].

Alternatively, by coating with a thin layer of carnauba wax (P21S), carefully controlling the amount of wax, the particles can be made neutrally buoyant in water. The amount of wax can be adjusted if the liquid is of different density. The advantage of coating the particle with wax is that the P21S carnauba wax aggregate was proven not to dissolve after 10 hours in water. Therefore the modified density can be stable throughout the duration of the experiment. However, to coat many particles with wax can be time-consuming while it is easy to add salt into the circulating water, and the same solution can be used for many particle tracking experiments. In this work the density of the salt solution was adjusted and verified by stirring the solution containing lots of tracer beads of various sizes. If the tracer beads followed the stirred flow without sinking or floating for a few minutes, the salt solution was considered of the same density of the tracer beads.

The disadvantage of the salt solution is that the affinity of the Cl ion to the functional group of the resin is stronger than the ^{18}F ion [15], and thus the ^{18}F ions bound to the resin bead would be exchanged by Cl ions. During several minutes of immersion, the bead could lose radioactivity significantly due to loss of ^{18}F ions. The ^{18}F ions would spread into the solution, which also increases the noise. The decrease of signal and increase of noise together pose a data processing challenge. In this study, the particle tracking algorithm used in Ref. [10, 11, 12] is further developed for tracking particle in this difficult situation and the tracking is further improved by adding filters. These improvements

in the tracking algorithms are an important part of the work reported in this paper.

2.3 Sensor arrays and positioning algorithm

As discribed in Sect. 1, the positron emanating from the nucleus annihilates with an electron nearby, which produces the back-to-back emitted gamma rays. The position of the isotope carrier, i.e. the labelled tracer, can be identified by firstly detecting the gamma photon pairs, secondly drawing LORs between detector pairs, and then finding the cross-points of many LORs in two dimensions at a time. In these experiments, gamma-ray sensor arrays (Siemens 3-ring TruePoint PET camera) were arranged to enclose a cylindrical cavity, as schematically shown in Fig. 4. Due to the cylindrical arrangement, any gamma photons passing at large angles to the camera z-plane will not be detected. The camera's axial length is 164 mm and the diameter is 855.2 mm, as shown in Fig. 4.

The dimension of each gamma-ray detector is 4 mm×4 mm×20 mm. There are 39 detectors in the axial direction, and 624 detectors on the circumference (see Fig. 4), so that the total number of detectors is 24336. Two gamma photons, if detected within a short time window, which is 4.5 ns for the TruePoint PET camera, are identified as being generated from one annihilation. The camera continues recording the information of detector pairs, and places a timing tag once every millisecond in the data stream.

More than one annihilation taking place in a coincidence window can cause more than two photons being counted, namely multiple coincidence, or can cause one of the photons from each annihilation to be counted, namely random coincidence, which results in mis-assigned LORs, as schematically shown in Fig. 5 events 1 and 2. More than this, there are other effects causing the LOR deviating from its exact position, e.g. scatter due to Compton interaction (see Fig. 5 event 3), and depth-of-interaction of the photons within the detectors (see Fig. 5 event 4) [2]. Therefore data processing algorithms capable of eliminating the false LORs and reducing the influence of deviating LORs would greatly increase the precision of positioning.

There are many strategies to denoise. Several algorithms have been developed, considering different experimental conditions, data quality, and processing speed. The algorithms to locate the particle and denoise can be categorized by processing LORs or 2-D cutpoints, i.e. intersection points, of LORs. The ones used for processing the data in this paper, working on the cutpoints of LORs, were evolved from the algorithm developed by Hoffmann et al. in Ref. [19]. The algorithm firstly finds out all the LORs and then all the coordinates of 2-D cutpoints using the sensor positions recorded as list-mode data in the PET camera. The 2-D average of all the cutpoint coordinates is then
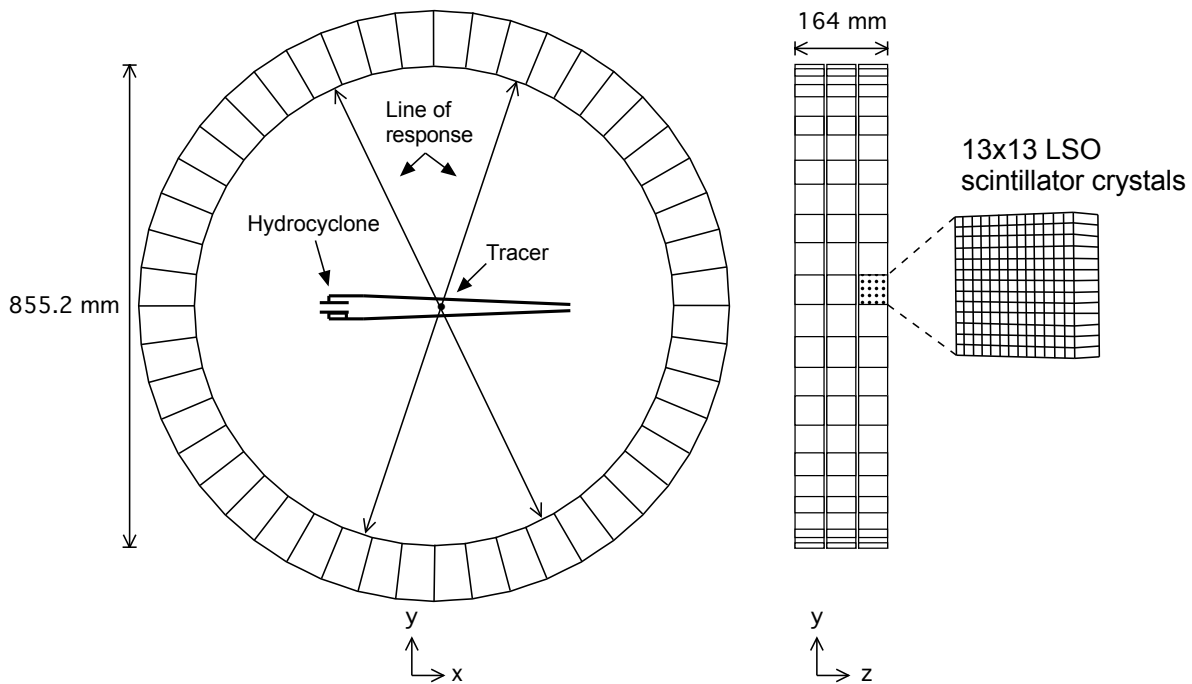
Fig. 4 Left: The hydrocyclone enclosed by the Siemens 3-ring TruePoint PET camera. The axis of the 3-ring is in the z-direction. Each ring has 48 blocks. The two photons are considered to have emanated from one annihilation if they are detected within a narrow time window. Right: Looking from the centre of the camera towards detector faces. Each block has 13×13 Lutetium Oxyorthosilicate (LSO) scintillator crystals.
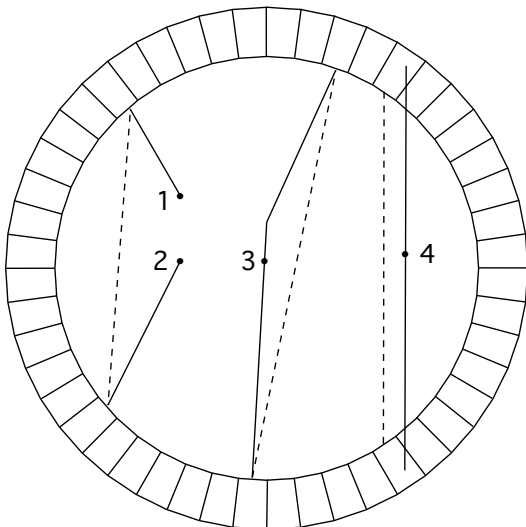

Fig. 5 Events 1 and 2: Two unrelated events with only one of each photon pair being detected within a defined time window, which leads to an incorrectly assigned LOR (dashed line). Event 3: One of the gamma photons is scattered leading to falsely assigned LOR. Event 4: The deviating LOR due to the depth-of-interaction of the photons within the detectors.

calculated. The cutpoints that are obviously generated by wrong LORs are eliminated by discarding those far away from this first average. The rest cutpoint coordinates are averaged the second time and then those farther than a specific distance from this average point are rejected from the next averaging. The process of averaging and discarding

is repeated until the spatial window has been narrowed to an optimized size, normally below 20×20 mm² [11]. The position of the particle in 2-D is then determined by averaging of the cutpoints remaining in the optimized window, of which the optimization is verified by the lowest standard deviation of the positions of a stationary tracer. The coordinate of the particle on the third axis is then obtained by simple averaging of the cutpoints between the LORs remaining after the above process.

As shown in Ref. [10] the more the cutpoints, the more precise the positioning. The number of cutpoints contributing to the final average depends on the activity on the particle and also, to an extent, on the location of the particle in the field of view (FOV) of the PET camera. Therefore, better labeling and centering the region of interest in the FOV would significantly improve the reliability of the data. In this work, how the number of cutpoints affect the resolved tracer trajectories will be elucidated and discussed.

Since the tracer forms a trajectory, rather than randomly appears in the space, it is possible to search for a position only around the position in the previous time step, rather than take all cutpoints in the FOV into account for every positioning process. The method finds the first particle position using the method described above. Once the first particle position has been determined, and the number of cutpoints in the final window is found to be sufficient for accepting the point, in the following time interval, the method takes the just-obtained position as the first average,

and then averages only the cutpoint coordinates within a window much smaller than the dimension of the FOV. Because the process of averaging and discarding needs to be preformed only twice or three times, the program can execute much faster. And because in this way most of the faulty cutpoints are disregarded right from the start, the precision of positions can be improved.

2.4 Data processing: smoothing

In addition to improving the positioning algorithm to avoid the interference of noise, smoothing, as post-signal processing, can also remove noise from signals. There are multiple smoothing methods that work differently depending on the nature of the signal and the noise. In the PEPT experiments, one or more tracers left in the flow loop can cause mis-positioning if using the single-tracer algorithm described in this paper. But this problem can be avoided by the adjacent-search algorithm as described in Sect. 2.3. The remaining noise is likely due to radioactivity leaching into the solution and the other causes of scattering inherent to the process [11], so the noise would be normally distributed rather than appear as localized spikes. Four smoothing methods were used for removing or mitigating this kind of noise as described below.

2.4.1 The weighted adjacent-averaging method

The weighted adjacent-averaging method averages the data around each point within the moving window using a parabolic weight with the weight area normalized to 1 [30].

2.4.2 The Gaussian filter method

The Gaussian filter method averages the data around each point weighted with a Gaussian function, normalizing the weight factors to sum to precisely one. It acts as a lowpass frequency filter, removing high frequency noise. The Gaussian function in 1-D has the form:

$$G(x) = \frac{1}{\sigma\sqrt{2\pi}}e^{-(x-\mu)^2/2\sigma^2} \qquad (4)$$

where σ is the standard deviation of the distribution and the distribution has a mean of μ (i.e. it is centered on the line x=μ).

Larger standard-deviation Gaussians produce higher degree of smoothing. The Gaussian filter outputs a "weighted average" of each datum's neighborhood, with the average weighted more towards the value of the central data, in contrast to the uniform moving average method. Because of this, a Gaussian filter provides gentler smoothing and preserves turns and features better than a similarly-sized mean filter.

2.4.3 The FFT (fast Fourier transform) filter method

Supposedly the particle moves smoothly along the time and the radioactivity in the surrounding solution super-imposes high-frequency fluctuations on the positions. The high-frequency noise can be removed by the FFT filter method [30]. Firstly, the Fourier transform of the positions is computed. Then the transformed data is multiplied with a parabolic low-pass window in the frequency domain. Frequencies higher than or equal to the cutoff frequency will be discarded. Finally, the altered frequencies are converted back to positions in time domain by taking the inverse Fourier transform.

2.4.4 The Savitzky-Golay method

The Savitzky-Golay method performs a polynomial regression to the data points in the moving window and replace the datum with the value of the polynomial at the position [31]. Compared to the adjacent-averaging method, the Savitzky-Golay method is superior in preserving features of the data, such as peak height and width. Increasing the window size, i.e. number of data points used in each local regression, can increase the smoothness of the result.

3 Results

While the results in this paper, as mentioned before, show tracking under particularly challenging circumstances we would like to point out that under more "normal" conditions, i.e. with the tracer particle in pure water (where there is negligible leaching) or in air, it is now possible, using our hardware and positioning algorithms, to obtain the position of the tracer centroid once per millisecond with a standard deviation of less than 100 μm in all three coordinate directions.

3.1 Positioning method comparison

Two methods were used to find the particle position in every time interval. The first one, referred to as "method 1" takes all cutpoints into account in the beginning of every positioning process, assuming no spatial relation between consecutive positions. The second method, referred to as "method 2," takes advantage of the fact that consecutive positions are spatially close, and thus seeks a given position only around the previous position, saving computation time. The experimental conditions and the number of cutpoints in the final 16^3 mm^3 window of all the particle tracking experiments shown in this paper have been listed in Table 1. The data processing time of "method 2" is in general one third of the time that "method 1" would require. The time

difference varies depending on the noise, which lengthens the time of "method 1," as well as the size of the spatial window that "method 2" uses to start the "averaging and shrinking window" process.

Fig. 6 (a) and (b) were obtained using method 1 and 2, respectively. The positions were obtained every millisecond. The volumetric flow rate was measured around 3.03 m^3/hour, that gives an average speed at the cyclone inlet of around 3.23 m/s, which is close to the speed at the inlet calculated using coordinates obtained by PEPT. The particle flows out through the overflow outlet because it follows the fluid flow path, which is in contrast to the trajectories shown in Ref. [10], where a density difference exists between the particle and carrier fluid. Method 1 gave an average number of cutpoints of 16793 in the final 16^3 mm^3 window, and method 2 an average number of 17333 in the final window, which means method 2 is superior in finding the region enclosing the most concentrated cutpoints, and thus method 2 should give a more reliable trajectory. As shown in Fig. 6, method 1 and method 2 produced similar trajectories but method 2's trajectory is smoother. The relative position of the trajectory in the hydrocyclone is sketched at the bottom of Fig. 6.

The temporal resolution can be increased by sectioning the detector-pair record for each millisecond in the data stream. In Fig. 6 (c) a position was obtained every half millisecond and the average number of cutpoints in the final window is noted in the bracket in Table 1. While the temporal resolution is improved, the uncertainty of positioning can also increase due to less available cutpoints.

In another experiment as shown in Fig. 7, the overall trajectory given by method 2 in (b) is obviously smoother than method 1's result shown in (a).

Although the two methods show roughly similar particle routes, method 1 can occasionally produce very wrong results like the obviously wrong coordinate shown in Fig. 8 (a). As the signal-to-noise ratio is low, method 2 becomes significantly better in isolating the true data from similarly intensive noise.

The standard deviation of particle position, representing the precision of positioning, is inversely proportional to the root of the number of LORs [10]. As the number of LORs decreases to a certain low level, the uncertainty of positioning would increase significantly. Fig 9 shows that, as the number of cutpoints enclosed in the final 16^3 mm^3 window is around 300, which is the result of low numbers of LORs in general, the tracer was positioned with great uncertainty and the track looks erratic even when method 2 is used.
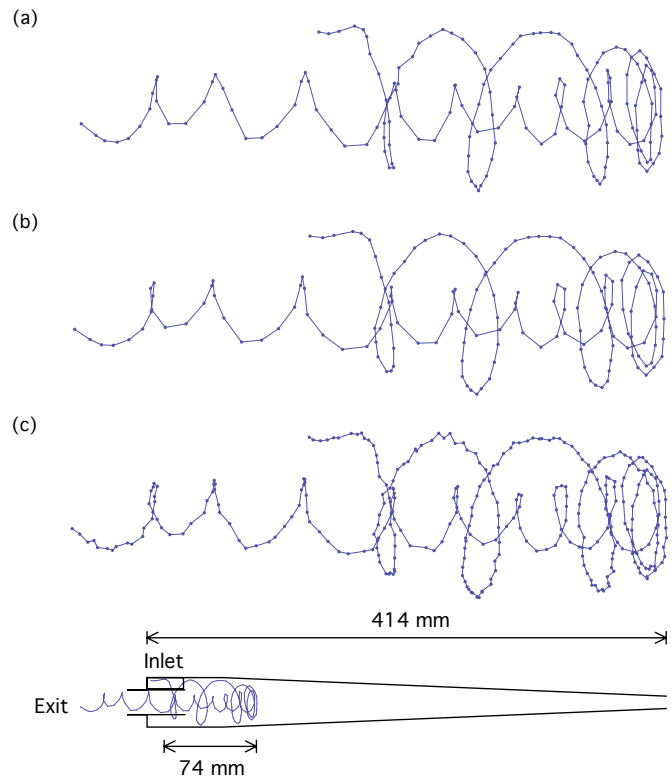

Fig. 6 (a) Trajectory obtained using "method 1" that takes all cutpoints into account in the beginning of every positioning process. Positions were obtained once per ms. (b) Trajectory obtained using "method 2" that finds next position only around the previous position. Positions were obtained once per ms. (c) Trajectory obtained using "method 2." Positions were obtained once per 0.5 ms. Trajectory duration: 166 ms.
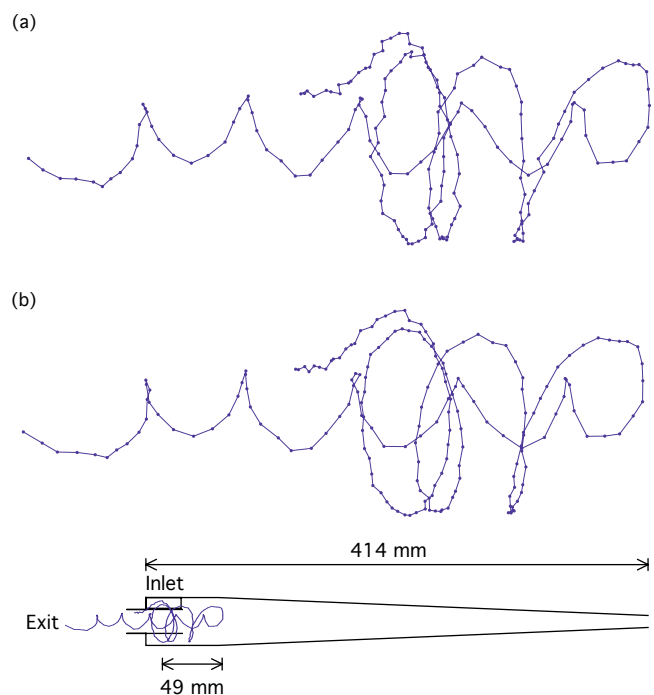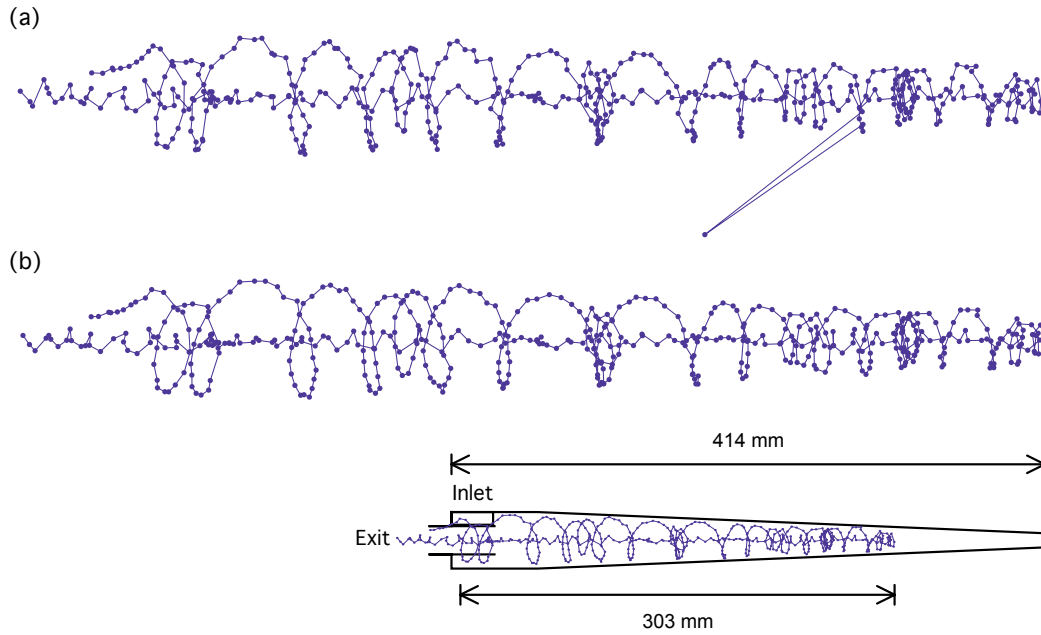

Fig. 7 (a) Trajectory obtained using method 1. (b) Trajectory obtained using method 2. Trajectory duration: 190 ms.

Table 1 Experimental conditions and number of cutpoints in the final 16^3 mm^3 window

Experiment	Flow rate (m³/hour)	Flow speed at the inlet (m/s)	Underflow rate (m³/hour)	Underflow/total flowrate	Number of cutpoints obtained by method 1 in the final window	Number of cutpoints obtained by method 2 in the final window
Fig. 6	3.03	3.23	0.49	16%	16793	17333 (4326)
Fig. 7	2.04	2.17	0	0%	9336	9637
Fig. 8	3.40	3.62	0.17	5%	995	1129
Fig. 9	3.06	3.25	0.14	5%	248	317

Fig. 8 (a) Trajectory obtained using method 1. (b) Trajectory obtained using method 2. Trajectory duration: 505 ms

3.2 Flow pattern

A code was developed in-house to determine the axis of the cyclone as the line minimizing the sum of the squared distances of the points from the line for the segments where the tracer particle was within the separation space. The original Cartesian coordinates of tracer positions can then be transformed to cylindrical coordinates once the cyclone axis is found. Further, the radial, tangential, and axial velocity can be calculated. Fig. 10 (a) shows the tracer's rotating around the computed cyclone axis located in the center of the graph and directed perpendicular to the paper, confirming the validity of the axis-finding algorithm and its implementation.

As described in Sect. 1.3, the tangential velocity in a cyclone at given radius can be calculated using Eq. (3), assuming the swirl velocity at the wall being equal to the inlet velocity. Barth, who pioneered some of the best early practical developments in cyclone modeling, considered that in some geometries the wall velocity can be much higher than the inlet velocity, and therefore proposed calculating the wall velocity from the inlet velocity using an empirical

obtained value α–the ratio of the moment-of-momenta of the fluid in the inlet and the fluid flowing along the wall [4, 18]:

$$\alpha \equiv \frac{v_{in}R_{in}}{v_{\theta w}R} \tag{5}$$

where v_{in} is the inlet velocity and $v_{\theta w}$ is the tangential wall velocity. R_{in} and R are cyclone dimensions as shown in Fig. 11.

In the cyclone with a "slot" type of rectangular inlet, just as the one used in the current study, the inlet jet is compressed against the wall, resulting in a decrease in the area accessible for the incoming flow. It was hypothesized that the tangential velocity at the wall and in the entire space between the wall and the vortex finder can be higher than the inlet velocity.

As shown in Fig. 10 (b), an increase in tangential velocity after the fluid entering the cyclone has been observed by PEPT, where the distances between two adjacent points right after entering the cyclone are longer than those in the inlet slot.

The average inlet velocity v_{in} calculated by averaging the first three ms in Fig. 10 (b) is 3.72 m/s and $v_{\theta w}$ calculated by
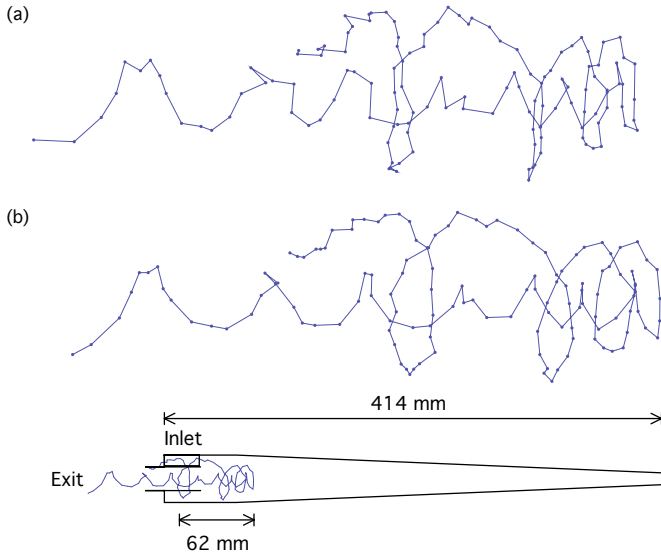
(a)

(b)

414 mm

Inlet

Exit

62 mm

Fig. 9 (a) Trajectory obtained using method 1. (b) Trajectory obtained using method 2. Very low activity on the tracer particle. Trajectory duration: 131 ms

averaging the first three ms right after entering the cyclone is 5.06 m/s. Substituting v_{in} and $v_{\theta w}$ and the dimensions of the cyclone into Eq. (5) gives α as 0.57.

Muschelknautz gave algebraic relations for α [27]:

$$\alpha = 1 - 0.4 \left(\frac{b}{R} \right)^{0.5} \tag{6}$$

which is reported to be valid for slot-type inlets with the ratio of inlet to outlet cross-sectional areas in the range 0.9 to 1.8. For the hydrocyclone used, the inlet to outlet cross-sectional area is 1.2 and the α calculated by Eq. (6) is 0.73.

Note that as shown in Fig. 10 (b) the tangential velocity drops as the tracer flows a whole round and approaches the inlet. The average tangential velocity of the last three ms shown in Fig. 10 (b) is 3.56 m/s, and the average velocity at the similar angle, between 290 and 340 degree, in the second round is 3.39 m/s, both of which are smaller than the velocity in the inlet slot, 3.72 m/s. Plotting the tangential velocity value of the first two rounds as radius versus angle on a r-θ map, as shown in Fig. 10 (c), shows that the tangential velocity is lower as the tracer approaches the inlet: The tracer enters the cyclone tangentially at about 270 degree, flowing counterclockwise, and the tangential velocities from 240 to 30 degree are all higher than 4 m/s. However, the tangential velocities decrease to lower than 4 m/s from 340 to 290 degree, where the tracer approached the inlet. Thus the assumption that the tangential wall velocity can be higher than the velocity at the inlet slot and can be calculated from the inlet velocity using the value α in Eq. (5) may have to be refined.

As shown in Ref. [14, 21] the measured profiles of tangential velocity vs. radius are approximately uniform

with the cyclone height. In this work the tangential velocity of experiment Fig. 6 (b) vs. radius at all heights were plotted and are shown in Fig. 12. Starting from the cyclone wall, the tangential velocity increases as the radius decreases until reaching a maximum value at a radius between 8.19 and 9.45 mm, which is a bit smaller than the radius of the vortex finder. Velocity data of radii smaller than 8.19 mm are fitted with Eq. (1), giving a value of Ω of 0.77. Velocity data of radii larger than 9.45 mm are fitted with Eq. (3), where C and n are found to be 25.42 and 0.65, respectively.

Again, the cyclone axis of Fig. 8 (b) was found using the above-mentioned algorithm and program. Fig. 13 (a) shows the tracer's rotating around the computed cyclone axis located in the center of the graph and with a direction perpendicular to the paper. The tracer enters the cyclone at about 310 degrees in Fig. 13 (b) and flows counterclockwise. Fig. 13 (c) plots the tracer's tangential velocity value on a radial axis at the appropriate angular position. The tracer's acceleration after entering the cyclone and deceleration as approaching the inlet area can be observed in Fig. 13 (b) and (c).

Tangential velocity vs. radius at all height of trajectory Fig. 8 (b) is plotted in one graph as shown in Fig. 14 (a). The data of radii smaller than 1.37 mm are not included since the calculation of tangential velocity using two adjacent points is not meaningful as the tracer rotates at a very small radius. Velocity data of radii smaller than 4 mm are fitted with Eq. (1), giving Ω being equal to 1.52. Velocity data of radii larger than 4 mm are fitted with Eq. (3), where C and n are found to be 5.73 and 0.09, respectively. The choice of data range would affect the constant values obtained. However, the velocity distribution in Fig. 14 (a) is different from Fig. 12: As the radius decreases from the maximum of 20 mm at the cylindrical wall, the rate that the tangential velocity increases is less in Fig. 14 (a) than that in Fig. 12. The reason can be that a neutral density particle penetrating that deep into the cyclone separation space is likely to have moved rather close to the wall also in the conical section, as confirmed by Fig. 8, giving rise to lower swirl velocities at all of the radial positions.

Fig. 15 shows from top to bottom: the radial position and the radial, tangential, and axial velocities as functions of axial position of trajectory Fig. 8 (b). The top graph of radial position vs. axial position includes the whole flow path from inlet to the overflow outlet. The velocity component plots include only the flow from inlet to the axial turning point deep in the cyclone at axial coordinate about 303 mm. The radial positions show that the tracer occasionally decreases its rotation radius as it swirls in the outer vortex, probably due to localized turbulence. In these radius decreasing areas, the tangential velocity increases abruptly, forming spikes in the graph. Also, in these radius regions of decreased radial coordinate, the axial velocity suddenly becomes negative,
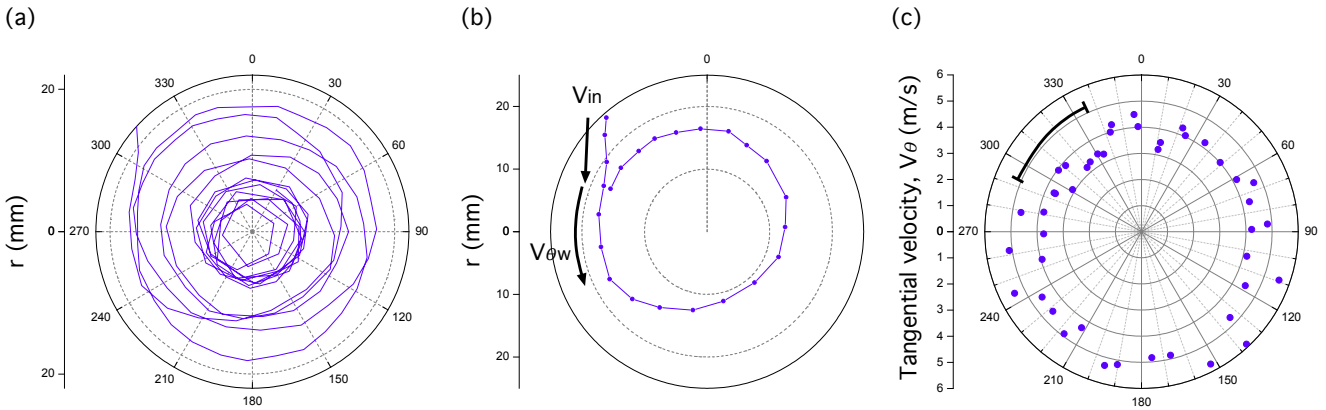
(a)   (b)   (c)

Fig. 10 ((a) r-θ plot of trajectory Fig. 6 (b). (b) First round of (a). (c) Tangential velocities of first two rounds as radii plotted at corresponding angles. The black curve covering the angles from 340 to 290 degree shows where the tangential velocity is lower as the tracer approaches the inlet at about 270 degree.
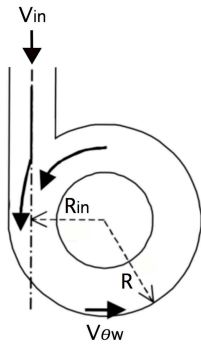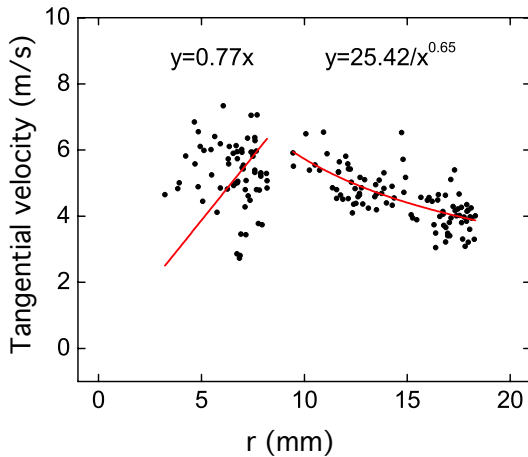

Fig. 11 Top view of the cyclone with a "slot" type of rectangular inlet.

Fig. 12 Tangential velocity vs. radius of Fig. 6 (b).

meaning that the tracer swirls towards the overflow outlet for the short period that it is in the "inner vortex."

The details of, and the relation between, the radial positions and velocity components can be seen more clearly by plotting as a function of time, as shown in Fig. 16. The dots are the data and the lines, indicating the trend, were obtained using the Savitzky-Golay smoothing with 20 points in a moving window and polynomial order of 2. Taking the

transparently shaded region around 150 ms as an example, while the radius decreases, the radial velocity accordingly becomes negative, the tangential velocity increases, and the axial velocity decreases to finally become negative. Difficulties in measuring radial velocity in hydrocyclones using LDV has been reported due to fluctuations of the radial velocity caused by precession of the vortex core or the air-core [6, 26] if present. Using PEPT the velocity components corresponding to the position and the time spent in the hydrocyclone can be measured in detail with high temporal and spatial resolutions.

3.3 Smoothing

Smoothing methods as described in Sect. 2.4 were applied to the particle trajectory shown in Fig. 8 (b).

Results of Gaussian filtering with standard deviations of 0.5 and 1 are shown in Fig. 17 (a) and (b), respectively. Larger standard deviation produces smoother trajectories, but the features showing the rotations in the inner vortex are also more blurred, i.e. the rotation in the inner vortex in Fig. 17 (b) is not as visible as in Fig. 17 (a).

Fig. 18 shows the smoothed trajectory using the FFT parabolic low-pass filter with cutoff frequency of 0.5 ms^{-1}. Features showing the particle's rotation in the inner core are better preserved compared to those obtained using other methods shown in Fig. 19 and Fig. 20. Cutoff frequencies lower than 0.5 ms^{-1} would produce smoother trajectories but at the same time blur the rotations in the inner core.

Fig. 19 shows the smoothed trajectory using the Savitzky-Golay method with 4 points in a moving window and polynomial order of 2. The particle's rotating along the cyclone wall becomes smoother, but the movement in the inner core is smeared.

Fig. 20 was obtained by the weighted adjacent-averaging method with 3 points in a moving window. The movement
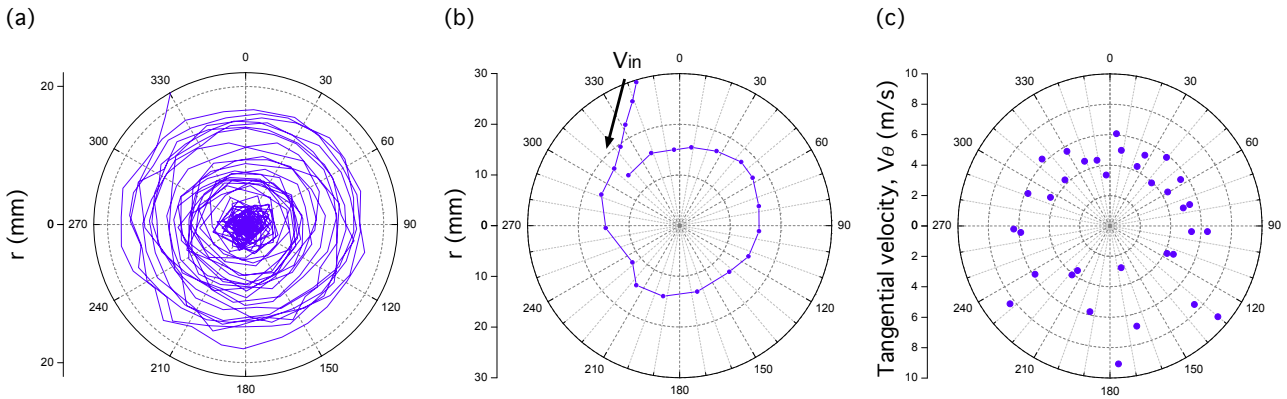
Fig. 13 (a) r-θ plot of trajectory Fig. 8 (b). (b) First round of (a). (c) Tangential velocities of first two rounds as radii plotted at corresponding angles.
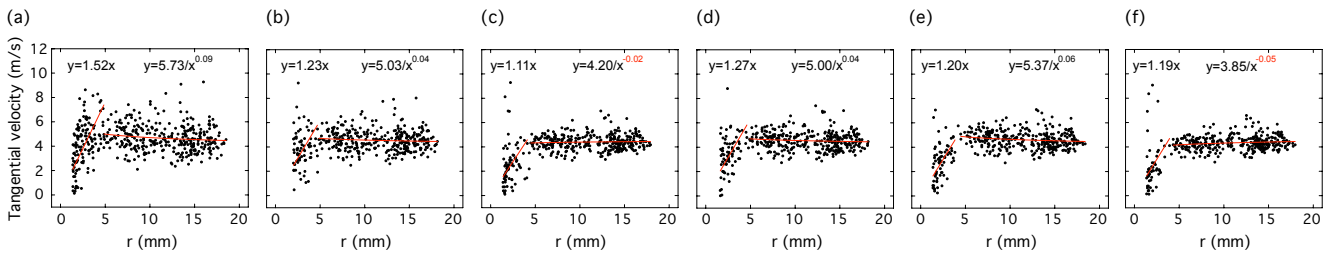

Fig. 14 Tangential velocity vs. radius plot of trajectory of (a) Fig. 8 (b), (b) Fig. 17 (a), (c) Fig. 17 (b), (d) Fig. 18, (e) Fig. 19, and (f) Fig. 20. The red exponents in (c) and (f) are minus, showing that the smoothing has reduced the higher tangential velocities and obliterated the characteristics of the "loss-free vortex" in the outer region of the cyclone as described by Eq. (3).

features in the cyclone inner core are nearly erased compared to those obtained by the other three methods.

A possible effect of smoothing is that the trajectory shrinks towards the cyclone axis. This effect is visible in Fig. 21 (c) and (f), where the rotation radii are reduced by "Gaussian filtering with standard deviation 1" and "weighted adjacent-averaging," respectively. The reduced rotation radii can be quantified by calculating the average of the radii from entering to leaving the cyclone, which is (a) 8.55, (b) 8.26, (c) 7.92, (d) 8.19, (e) 8.23, and (f) 7.74 for Fig. 21. The Savitzky-Golay method with a larger moving window would also pull the trajectory towards the axis.

Fig. 14 (b), (c), (d), (e), and (f) show the tangential velocity vs. radius of trajectories of Fig. 17 (a) and (b), Fig. 18, Fig. 19, and Fig. 20, respectively. Since the "Gaussian filtering with standard deviation 1" (Fig. 14 (c)) and the "weighted adjacent-averaging method" (Fig. 14 (f)) reduce the rotation radii, it would also reduce the tangential velocities, leading to further weakening the higher velocity. As a result, fitting the velocity in the outer region of the cyclone with Eq. (3) does not give the expected positive exponent, as marked red in Fig. 14 (c) and (f), showing that the characteristics of the "loss-free vortex" have been obliterated by smoothing.

The "Gaussian filtering with standard deviation 0.5," the "FFT parabolic low-pass filter method with cutoff frequency of 0.5 ms^{-1}," and the "Savitzky-Golay method with 4 points in a moving window and polynomial order of 2" all reasonably preserve the characteristics of the "solid-body rotation" in the centre and the "loss-free rotation" in the outer region of the cyclone. Therefor these three methods with such parameters are all considered applicable.

4 Conclusion

In this study the flow in a hydrocyclone was visualized by following the paths of neutral density particles mimicking liquid elements using positron emission particle tracking (PEPT). The PEPT technique has been refined making it possible to produce neutral-density tracer and tracking in a low-signal and high-noise condition. The developed data-processing algorithm has proven able to produce more reliable trajectories. The developed algorithm also allows improving the temporal resolution to positioning per 0.5 ms in such challenging conditions. The uncertainty in positioning was found to rise significantly when the radioactivity becomes so low that less than 1000 cutpoints are enclosed in the final spatial window for determining the tracer position per ms.
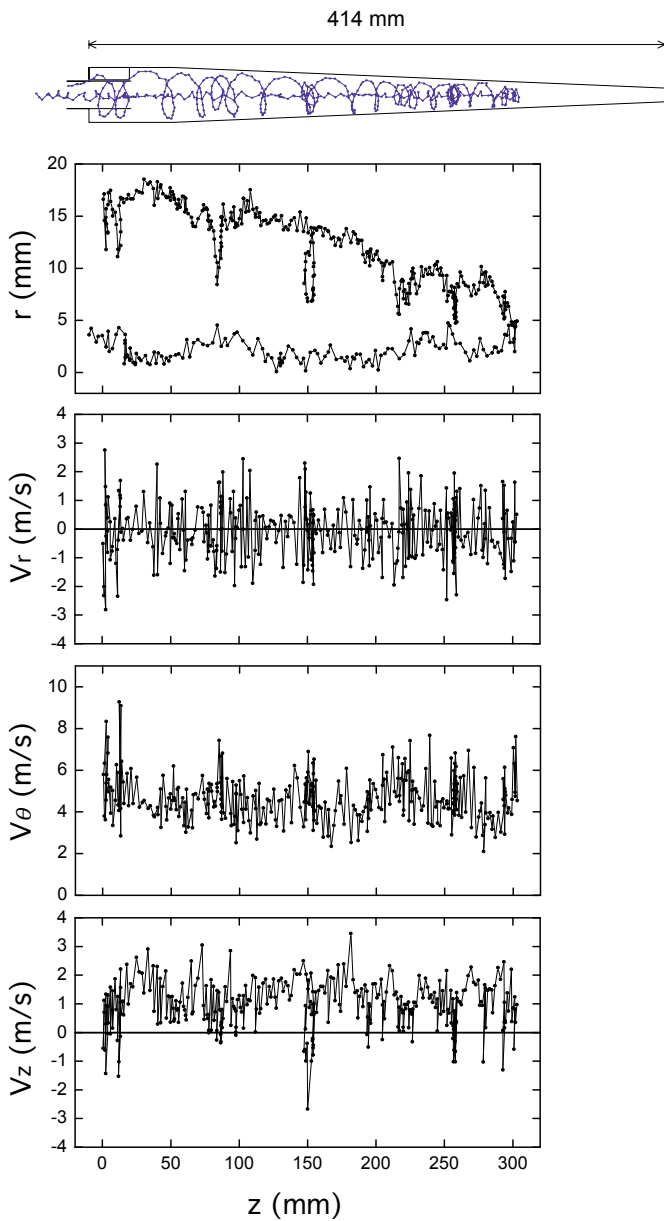
Fig. 15 Radial position and radial, tangential, and axial velocity as a function of axial position of trajectory Fig. 8 (b). The velocity component plots show data from inlet to the axial turning point deep in the cyclone at axial coordinate about 303 mm.

Fig. 16 Radial position and radial, tangential, and axial velocity as a function of time of trajectory Fig. 8 (b). Data from inlet to the axial turning point deep in the cyclone at axial coordinate about 303 mm are shown. The transparently shaded region around 150 ms shows an example of the relation between the radial positions and velocity components. While the radius decreases, the radial velocity accordingly becomes negative, the tangential velocity increases, and the axial velocity decreases to finally become negative. The similar correlation between the radial positions and velocity components can be observed in various temporal period.

Further data processing transforms the Cartesian coordinates to cylindrical coordinates and calculates the tangential, radial, and axial velocity components at every ms location. The effect of the slot inlet on the tangential velocity in the cylinder section was analyzed, showing fluid acceleration and deceleration due to the inlet geometry. As the tracer enters the cyclone, the tangential velocity increases as Barth theorized. However, the tangential velocity appeared to decrease to lower than inlet velocity as the tracer approaches the inlet area. Tangential velocity distribution as a function of radius conforms to and can be fitted by Alexander's
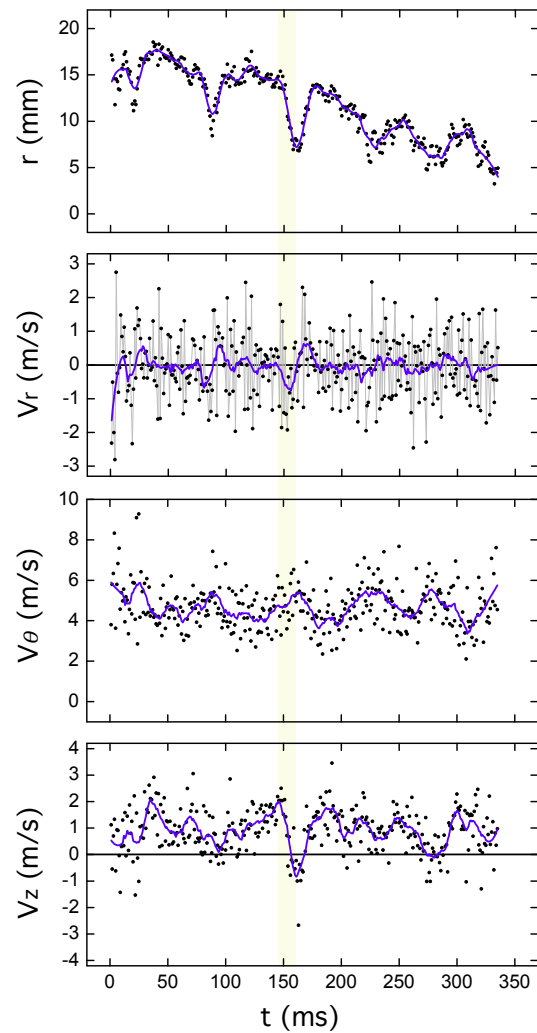
model: a near loss-free swirl surrounding a core of near solid-body rotation. The high-resolution position and velocity components obtained by PEPT reveals the possible turbulence in the hydrocyclone and account for the specifics of the velocity field and the movement of fluid elements in detail.

Various smoothing methods were applied to remove the effects of noise, which is likely due to radioactivity leaching lowering the signal-to-noise ratio. A Gaussian filter with appropriate standard deviation, the FFT parabolic low-pass filter with proper cutoff frequency, and the Savitzky-Golay method were found sufficient and able to preserve
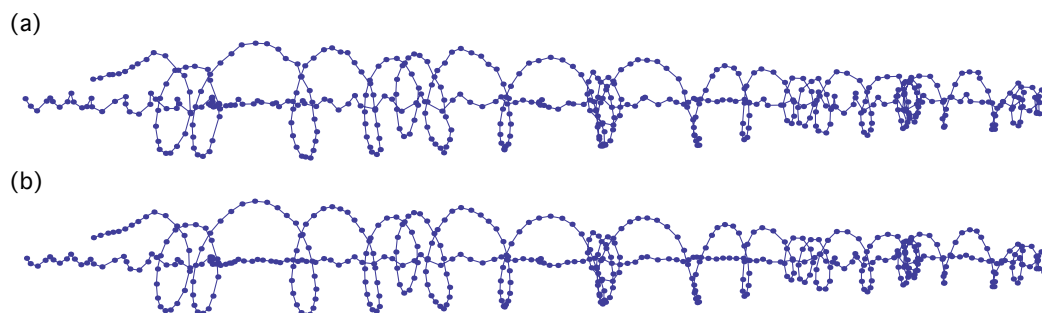
(a)

(b)

Fig. 17 Using the Gaussian filtering with a standard deviation of (a) 0.5 and (b) 1 to smooth the trajectory Fig. 8 (b).
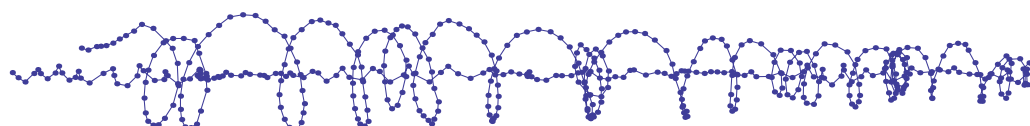
Fig. 18 Using the FFT parabolic low-pass filter method with cutoff frequency of 0.5 ms^{-1} to smooth trajectory Fig. 8 (b).
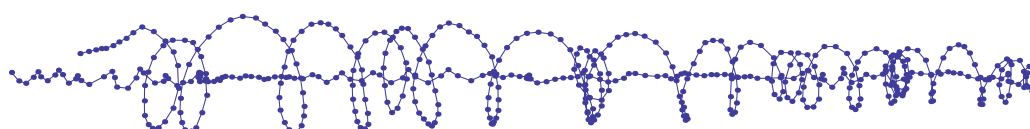
Fig. 19 Using the Savitzky-Golay method with 4 points in a moving window and polynomial order of 2 to smooth trajectory Fig. 8 (b).

the characteristics of the flow pattern, while the weighted adjacent-averaging method could lose important features of the velocity field. While both the Gaussian filter and the FFT filter are capable of removing the high frequency noise, the results show that the parameters have to be carefully chosen considering the principles of the methods and the nature of the data.

In this work PEPT has been successfully applied to study the flow of the continuous phase in a hydrocyclone by making the tracer neutrally buoyant. However, one should be careful in interpreting the trajectories if applying PEPT to study the hydrocyclones containing pulp fibers as the fiber network would disturb the movement of the particles.

We emphasize again that the tracking in this work was particularly challenging due to the nature of the fluid used and that in "normal" systems, e.g. with air or pure water as fluids, the algorithms used here can determine the particle centroid position with a standard deviation of less that 100 μm in all three coordinate directions.

References

1. Alexander RM (1949) Fundamentals of cyclone design and operation. Proceedings of the Australasian Institute of Mining and Metallurgy 152-153:203–228

2. Bailey DL (2005) Positron emission tomography: basic sciences. Springer

3. Barker A, Bock J, Lorenz R, Markl M (2010) 4D flow MR imaging. MAGNETOM Flash 2:46–52

4. Barth W (1956) Berechnung und auslegung von zyklonabscheidern auf grund neuerer. Brennstoff-Wärme-Kraft 8(1):1–9

5. Bergström J, Vomhoff H (2005) Application of a pitometer to measure the tangential velocity in a cylindrical through-flow hydrocyclone operated with a fiber suspension. Nordic Pulp and Paper Research Journal 20(1):30–35

6. Bergström J, Vomhoff H (2007) Experimental hydrocyclone flow field studies. Separation and Purification Technology 53(1):8–20, DOI http://dx.doi.org/10.1016/j.seppur.2006.09.019

7. Bergström J, Vomhoff H, Söderberg D (2007) Tangential velocity measurements in a conical hydrocyclone operated with a fibre suspension. Minerals Engineering 20(4):407–413, DOI http://dx.doi.org/10.1016/j.mineng.2006.09.008

8. Blaj O, Merzeau P, Snabre P, Pouligny B (2011) An automated single-particle tracker: application to characterization of non-azimuthal motion in couette flows at low reynolds number. Experiments in Fluids 50(6):1559–1570, DOI 10.1007/s00348-010-1013-y
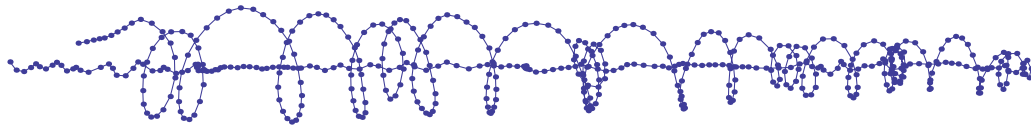
Fig. 20 Using the weighted adjacent-averaging method with 3 points in a moving window to smooth trajectory Fig. 8 (b).
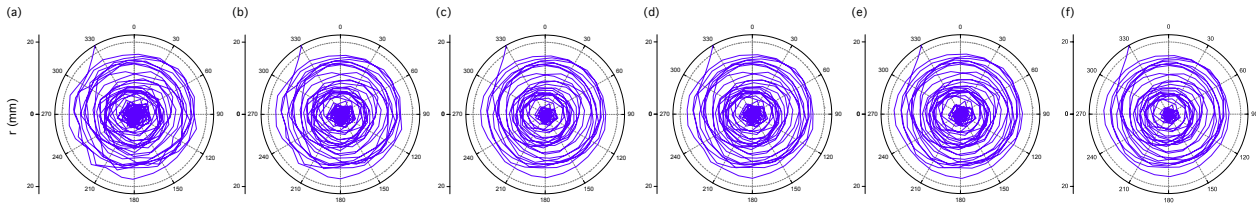

Fig. 21 r-θ plot of trajectory of (a) Fig. 8 (b), (b) Fig. 17 (a), (c) Fig. 17 (b), (d) Fig. 18, (e) Fig. 19, and (f) Fig. 20.

9. van Campen L, Mudde RF, Slot J, Hoeijmakers H (2012) A numerical and experimental survey of a liquid-liquid axial cyclone. International journal of chemical reactor engineering 10(1): A35

10. Chang YF, Ilea CG, Aasen ØL, Hoffmann AC (2011) Particle flow in a hydrocyclone investigated by positron emission particle tracking. Chemical Engineering Science 66(18):4203–4211, DOI DOI 10.1016/j.ces.2011.06.001

11. Chang YF, Adamsen TC, Hoffmann AC (2012) Using a pet camera to track individual phases in process equipment with high temporal and spatial resolutions: Algorithm development. In: 2012 IEEE International Instrumentation and Measurement Technology Conference (I2MTC), pp 2326–2330

12. Chang YF, Adamsen TCH, Pisarev GI, Hoffmann AC (2013) PEPT: An invaluable tool for 3-D particle tracking and CFD simulation verification in hydrocyclone studies. EPJ Web of Conferences 50:05,001p.1–p.8, URL http://dx.doi.org/10.1051/epjconf/20135005001

13. Cheng NS (2008) Formula for the viscosity of a glycerol-water mixture. Industrial & Engineering Chemistry Research Engineering Chemistry Research 47(9):3285–3288, DOI 10.1021/ie071349z

14. Dabir B, Petty CA (1986) Measurements of mean velocity profiles in a hydrocyclone using laser Doppler anemometry. Chemical Engineering Communications 48(4-6):377–388, DOI 10.1080/00986448608910025

15. Fan X, Parker D, Smith M (2006) Labelling a single particle for positron emission particle tracking using direct activation and ion-exchange techniques. Nuclear Instruments and Methods in Physics Research Section A: Accelerators, Spectrometers, Detectors and Associated Equipment 562(1):345–350

16. Fisher MJ, Flack RD (2002) Velocity distributions in a hydrocyclone separator. Experiments in Fluids 32(3):302–312, DOI 10.1007/S003480100344

17. Frisch U, Hoekstra AJ, Vliet E, Derksen JJ, Akker HEA (1998) Vortex core precession in a gas cyclone. Advances in Turbulence VII Fluid Mechanics and Its Applications 46:289–292

18. Hoffmann AC, Stein LE (2007) Gas cyclones and swirl tubes: principles, design and operation. Springer

19. Hoffmann AC, Dechsiri C, van de Wiel F, Dehling H (2005) PET investigation of a fluidized particle: spatial and temporal resolution and short term motion. Measurement Science and Technology 16(3):851–858

20. Hsieh KT, Rajamani K (1988) Phenomenological model of the hydrocyclone: Model development and verification for single-phase flow. International Journal of Mineral Processing 22(1–4):223–237, DOI http://dx.doi.org/10.1016/0301-7516(88)90065-8

21. Hwang CC, Shen HQ, Zhu G, Khonsari MM (1993) On the main flow pattern in hydrocyclones. Journal of Fluids Engineering 115(1):21–25, URL http://dx.doi.org/10.1115/1.2910106

22. Knowles SR, Woods DR, Feuerstein IA (1973) The velocity distribution within a hydrocyclone operating without an air core. The Canadian Journal of Chemical Engineering 51(3):263–271

23. Laverman JA, Fan X, Ingram A, Annaland MvS, Parker DJ, Seville JPK, Kuipers JAM (2012) Experimental study on the influence of bed material on the scaling of solids circulation patterns in 3d bubbling gas–solid fluidized beds of glass and polyethylene using positron emission particle tracking. Powder Technology 224(0):297–305

24. Lide D (2004) CRC Handbook of Chemistry and Physics: A Ready-reference Book of Chemical and Physical Data. CRC Handbook of Chemistry and Physics, 85th Ed, CRC Press

25. Lim EWC, Chen YR, Wang CH, Wu RM (2010) Experimental and computational studies of multiphase hydrodynamics in a hydrocyclone separator system. Chemical Engineering Science 65(24):6415–6424

26. Monredon TC, Hsieh KT, Rajamani RK (1992) Fluid flow model of the hydrocyclone: an investigation of device dimensions. International Journal of Mineral Processing 35(1-2):65–83

27. Muschelknautz E (1980) Theorie der fliehkraftabscheider mit besonderer berücksichtigung hoher temperaturen und drücke. VDI-Berichte 363:49–60

28. Parker DJ, Leadbeater TW, Fan X, Hausard MN, Ingram A, Yang Z (2008) Positron imaging techniques for process engineering: recent developments at Birmingham. Measurement Science and Technology 19(9):094,004

29. Pisarev GI, Gjerde V, Balakin BV, Hoffmann AC, Dijkstra HA, Peng W (2012) Experimental and computational study of the "end of the vortex" phenomenon in reverse-flow centrifugal separators. AIChE Journal 58(5):1371–1380, DOI 10.1002/aic.12695

30. Press WH, Flannery BP, Teukolsky SA, Vetterling WT (1992) Numerical recipes in C: The art of scientific computing. Cambridge University Press

31. Savitzky A, Golay M (1964) Smoothing and differentiation of data by simplified least squares procedures. Analytical Chemistry 36(8):1627–1639

32. Seo KW, Choi YS, Lee SJ (2012) Dean-coupled inertial migration and transient focusing of particles in a curved microscale pipe flow. Experiments in Fluids 53(6):1867–1877, DOI 10.1007/s00348-012-1403-4